crystals

MDPI

Article

Structural Degradation of O3-$NaMnO_2$ Positive Electrodes in Sodium-Ion Batteries

Matteo Palluzzi [1,†], Laura Silvestri [2,†], Arcangelo Celeste [1,†], Mariarosaria Tuccillo [1,†], Alessandro Latini [1,†] and Sergio Brutti [1,*,†]

[1] Dipartimento di Chimica, Sapienza Università di Roma, Piazzale Aldo Moro 5, 00185 Rome, Italy; matteo.palluzzi@uniroma1.it (M.P.); arcangelo.celeste@uniroma1.it (A.C.); mariarosaria.tuccillo@uniroma1.it (M.T.); alessandro.latini@uniroma1.it (A.L.)
[2] Dipartimento di Tecnologie Energetiche ENEA, C.R. Casaccia Via Anguillarese 301, 00123 Rome, Italy; laura.silvestri@enea.it
* Correspondence: sergio.brutti@uniroma1.it; Tel.: +39-0649913957
† These authors contributed equally to this work.

Abstract: In this manuscript, we report an extensive study of the physico-chemical properties of different samples of O3-$NaMnO_2$, synthesized by sol–gel and solid state methods. In order to successfully synthesize the materials by sol–gel methods a rigorous control of the synthesis condition has been optimized. The electrochemical performances of the materials as positive electrodes in aprotic sodium-ion batteries have been demonstrated. The effects of different synthesis methods on both structural and electrochemical features of O3-$NaMnO_2$ have been studied to shed light on the interplay between structure and performance. Noticeably, we obtained a material capable of attaining a reversible capacity exceeding 180 $mAhg^{-1}$ at 10 mAg^{-1} with a capacity retention >70% after 20 cycles. The capacity fading mechanism and the structural evolution of O3-$NaMnO_2$ upon cycling have been extensively studied by performing post-mortem analysis using XRD and Raman spectroscopy. Apparently, the loss of reversible capacity upon cycling originates from irreversible structural degradations.

Keywords: Na-ion batteries; positive electrode materials; $NaMnO_2$; post-mortem; Raman

Citation: Palluzzi, M.; Silvestri, L.; Celeste, A.; Tuccillo, M.; Latini, A.; Brutti, S. Structural Degradation of O3-$NaMnO_2$ Positive Electrodes in Sodium-Ion Batteries. *Crystals* **2022**, *12*, 885. https://doi.org/10.3390/cryst12070885

Academic Editors: Feng Yu, Teng Wang and Xinhai Yuan

Received: 19 May 2022
Accepted: 18 June 2022
Published: 22 June 2022

1. Introduction

Since their introduction in the 1990s, lithium-Ion Batteries (LIBs) have played a critical role in powering our daily lives thanks to their high volumetric and gravimetric energy [1]. LIBs are commonly used in portable electronic devices [2], and in the last decade, their demand has been increasing monotonically and is mainly driven by the automotive sector (electric vehicles) [3] and renewable-energy (power plants [4]). This extraordinary market success is challenging their main limit: Lithium is, in fact, not abundant on Earth, so it has become progressively more expensive [5]. In the last few years, many research groups investigated battery chemistry based on more common and cheaper elements (such as sodium, calcium, potassium or aluminum) [5]. Sodium is an excellent candidate thanks to its abundance, low cost and especially chemical resemblance to lithium. These properties allow the transfer of many principles already known for LIBs to Sodium-Ion Batteries (SIBs) [5].

Today, the research on SIBs is focused on the identification of host intercalation materials that are able to reversibly operate for hundreds of charge/discharge cycles. In fact, despite their similarity, sodium has a larger ionic radius compared to lithium (116 pm vs. 90 pm [5]), thus challenging the resilience of host lattice during intercalation reactions.

Focusing on positive electrodes, one of the most studied family of materials is the layered transition metal oxides (LTMOs) [6,7]. While for lithium, the only LTMOs that achieve a reversible intercalation are $LiCoO_2$, $LiNiO_2$ and their solid solution; for sodium,

basically all LTMOs can achieve a reversible intercalation [8,9]. One of the most interesting sub-classes are LTMOs based on manganese (Na_xMnO_2) thanks to their large theoretical capacity, environmental benignity and facile synthesis [6,7].

Sodium-manganese oxides (Na_xMnO_2) have been studied since the 1970s: these materials exist in many different stoichiometries and structures [10]. They are fundamentally composed by MnO_6 octahedra arranged in double or triple chains (generating tridimensional tunnel-structures) or in bidimensional layers (generating layered structures) depending on the sodium content (i.e., $Na/Mn < 0.5$ tunnel structures and $Na/Mn > 0.5$ layered structures) [10,11]. Usually, layered Na_xMnO_2 (NMO) with a Na/Mn ratio around 0.6–0.7 belongs to a P2-type phase based on the classification for LTMOs made by Delmas, whereas materials with a Na/Mn ratio close to unity belong to an O3-type phase (referred as α-$NaMnO_2$, *C2/m*) or to an orthorhombic buckled distortion (referred as β-$NaMnO_2$, *Pmmn* or *Pmnm*) [11,12].

The use of NMO in sodium batteries has been discussed in the literature previously. In particular, most authors focus on the layered NMO with P2-type structure that can deliver theoretical capacities around 160–180 mAh/g but shows practical values below 100 mAh/g. Typically, P2-NMO are synthesized by a wide variety of methods, especially sol–gel [13–26] to allow the careful tuning of crystallite morphology and size.

On the contrary, few studies tackle NMO belonging to O3-type structure, despite their larger theoretical capacity, i.e., 240 mAh/g, compared to P2 materials. Apparently O3-NMOs can be synthesized only by solid-state methods that allow a limited control on synthesis parameters compared to sol–gel. In fact, sol–gel routes can be finely tuned to drive specific crystal morphologies, particle coatings and defects by assessing many independent synthesis parameters (e.g., gelification agent, gel aging, precursor ratio, precursor nature, gelling temperature, annealing conditions, gel formation solution composition and solvation environment).

In the Table 1, α-$NaMnO_2$ and β-$NaMnO_2$ literature performance in aprotic sodium batteries are compared in terms of real capacities delivered in discharges at 1 and 20 as well as the extent of the galvanostatic cycling range. All figures for O3-NMO are beyond those of P2-NMO, despite the poor comprehension of the interplay between structure/morphology and battery performance [27]. On the other hand, in all the literature reports, O3-NMO shows a remarkable capacity fading leading to capacity retentions after 20 cycles of about 70–80%: the origin of this huge loss of capacity is still unknown.

In this study, we report the synthesis of $Na_{1-x}MnO_2$ with an O3 structure using sol–gel methods [28] and their ability to reversibly work in sodium-ion batteries using an aprotic electrolyte in comparison to a solid-state benchmark material. Our aim is to illustrate the close interplay between battery performance and physicochemical properties such as structure, morphology and composition. The final goal of this manuscript is to shed light on the O3-NMO deactivation mechanism to understand what drives capacity fading upon cycling. Overall, here, we report two main innovative elements: (a) the viability of sol–gel routes to synthesize O3-NMO and (b) the occurrence of structural evolution upon cycling leading to phase segregation and performance fading.

Table 1. Results from studies about O3-type $NaMnO_2$ (and its orthorhombic distorted equivalent) used as cathode in SIBs [11,29–35].

Stoichiometry	Space Group	i (mAg^{-1}) C-Rate	OCV (V)	Q^{1st}_{disch} ($mAhg^{-1}$)	Q^{20th}_{disch} ($mAhg^{-1}$)	N. of Cycles	Ref.
$NaMnO_2$	*C2/m*	70 ($\mu A/cm^2$)	*ca.*3.5–1.4	*ca.*54			[11]
	Pmmn	70 ($\mu A/cm^2$)	*ca.*3.5–1.7	*ca.*37			
	Pmnm	10	2.0–4.2	190	*ca.*170	100	[29]
		50	2.0–4.2	*ca.*170	*ca.*150	100	
		400	2.0–4.2	142	*ca.*120	100	
		2000	2.0–4.2	90	*ca.*80	100	
	C2/m	10	2.0–3.8	175			[30]
		100	2.0–3.8	*ca.*85	*ca.*60	50	
	Pmmn	10	2.0–3.8	134			
		100	2.0–3.8	*ca.*95	*ca.*80	50	
	C2/m	24	2.0–3.8	185	*ca.*130	20	[31]
		8	2.0–3.8	194		10	
	C2/m	100	1.5–4.2	*ca.*125	*ca.*75	50	[32]
		200	1.5–4.2	90			
		1000	1.5–4.2	30			
	C2/m	C/5	1.7–4.0	146	*ca.*110	20	[33]
	C2/m	12	2.0–3.8	169	*ca.*110	20	[34]
	C2/m	10	*ca.*1.2–4.5	*ca.*180	*ca.*100	20	[35]

2. Materials and Methods

2.1. Synthesis

Sodium manganites have been prepared using a sol–gel method. Manganese(II) acetate ($(CH_3CO_2)_2Mn{\cdot}4H_2O$, Sigma-Aldrich (St. Louis, MO, USA)) and sodium carbonate (Na_2CO_3) were mixed in a 2:1 ratio and dissolved in a minimum quantity of water under stirring. Oxalic acid ($C_2O_4H_2{\cdot}2H_2O$) was added with additional water to ensure its dissolution. The pH was then adjusted to 8 adding a 28% ammonia solution. The solution was heated to 80 °C and maintained under continuous stirring until a gel was obtained. The gel has been transferred in a drying tube and kept at 200 °C and low pressure (under 100 torr) for 18 h. The product obtained has been manually ground and annealed at 720 °C for 12 h using a heating rate of 1 °C/min and finally quenched to room temperature in a vacuum chamber. After cooling to room temperature, the sample was directly transferred to an Ar-filled glove-box and manually ground in an agate mortar. The final product has been stored in the glove-box due to its sensitivity toward air moisture [9] and was identified as NM-SG.

Two additional samples have been prepared using the same sol–gel method but adding a 5% and 10% sodium excess. These samples are identified as NM5-SG and NM10-SG.

We would like to stress that many alternative synthesis conditions have also been checked mainly using different annealing temperatures and heating rates: apparently, only the here reported synthesis parameters allowed the obtainment of samples with minimal contaminants.

In addition to sol–gel, a benchmark sample has been synthesized following a solid-state method based on the literature [30]. Sodium carbonate (Na_2CO_3, Sigma-Aldrich) and manganese(II) oxide (Mn_2O_3, Sigma-Aldrich) have been mixed in a 1:1 ratio and manually ground. The mixed powders have been annealed at 700 °C for 6 h using an heating rate of

2.5 °C/min and then cooled to room temperature. The powder obtained has been manually ground again and a second annealing has been performed: this time at 700 °C for 20 h using a heating rate of 10 °C/min. The sample has been quenched to room temperature in a vacuum chamber, and after cooling to room temperature, it has been directly transferred to an Ar-filled glove-box and manually ground in an agate mortar. The final product is identified as NM-SS.

2.2. Characterization Methods

X-ray diffraction (XRD) characterization of the samples has been carried out using a Philips X'Pert PRO diffractometer (Cu-K_α radiation source with a wavelength λ = 1.54 Å) in the 2θ range 10–90°, with a step-size of 0.00836° and a speed of 0.01°/s. Rietveld refinement procedures have been carried out on the diffractograms obtained using GSAS-II routines [36]. The O3 structure retrieved from Ref. [30] has been used as starting point. The cell parameters (a, b, c and β), the atomic positions and oxygen vacancies have been optimized together with uniaxial size and strain to mimic peak broadening. GSAS-II exploits a modified Warren–Averbach algorithm to estimate size and strain from the peak broadening trends while also considering the instrumental broadening. Antisite defects have been estimated by refining Na/Mn intermixing between the *2a* and *2d* atomic sites, keeping their ratio constant.

The morphology of the samples has been investigated by scanning electronic microscopy (SEM) using an AURIGA-ZEISS instrument. The micrographs obtained have been analyzed using the program ImageJ [37]. Moreover, Energy-dispersive X-ray (EDX) spectroscopy experiments have been carried out during SEM acquisition.

Raman spectroscopy has been performed using a DILOR LabRam HR Raman Microscopy with a He-Ne (632.9 nm) laser source and a CCD Peltier-cooled detector.

To ensure the protection of the samples from air during XRD and Raman experiments, specific protocols have been implemented. XRD samples have been protected using a Kapton® film. Raman samples have been first sealed in a capsule made of steel with a glass window to allow visible light transmission.

2.3. Electrochemical Methods

The preparation of casted electrodes has been carried out in a dry room. Mixed powders have been prepared manually grounding the active materials, superP carbon (Timcal) and PVDF (Solef) binder in a weight ratio of 8:1:1. 1-Methyl-2-pyrrolidinone (NMP, Sigma-Aldrich) has been added in a minimal quantity to ensure the dissolution of PVDF, and the suspensions obtained have been doctor-bladed on aluminum foils. The filmed foils have been dried at 50 °C under vacuum for 3 h and then cut in disks with diameter of 10 mm (and an active material loading of 1.8–3.6 mg/cm^2). Electrodes have been dried again in a drying tube at 60 °C in dynamic vacuum for three hours and stored in the glove-box.

Sodium cells have been assembled in the glove box using El-Cell Std laboratory cells. Electrodes have been coupled with fiberglass separators (Whatman) and sodium metal disks. The electrolyte used is a solution 1M sodium bis(trifluoromethanesulfonyl)imide (NaTFSI) in propylene carbonate (PC) with 3% wt of fluoroethylene carbonate (FEC), in which the separators were soaked (Solvionic).

Galvanostatic cycling (GC) and cyclic voltammetry (CV) have been used to characterize battery performance at room temperature.

GC has been performed at 10 mA/g (C/24 in terms of C-rate) in the range between 1.8 and 3.7 V (or 1.7–3.6 in the case of NM10-SG) using an MTI 8-channel Battery Analyzer.

CV has been performed at different scan rates (1, 0.2 and 0.05 mV/s) in the range between 1.8 and 4 V by a potentiostat IVIUM-VERTEX.

After 20 charge/discharged cycles, the cells utilized for GC have been stored in the glove-box and disassembled, and the electrodes have been carefully collected. Post mortem electrodes have been washed twice using dimethyl carbonate (DMC) and once using

tetrahydrofuran (THF), and then they were dried under vacuum for about half an hour. Dried electrodes have been cut into pieces and analysed by XRD and Raman spectroscopy.

3. Results and Discussion

3.1. Synthesis of O3-NMO

A summary of the samples, their synthesis conditions and their experimental stoichiometries is reported in Table 2. The sample compositions have been estimated starting from the Na/Mn experimental ratio and assuming general stoichiometry ($Na_{1-x}MnO_2$). The oxygen content that cannot be estimated reliably from EDX has been kept constant per formula unit in consideration of the facile Mn^{+4} formation at high temperatures [38]. All samples show a Na/Mn ratio below 1, suggesting sodium loss during the annealing at high temperatures [29,30,32,34]. In the literature, larger Na/Mn ratios, even close to unity, have been reported: However, these stochiometric O3-$NaMnO_2$ phases can be apparently obtained only using large amounts of sacrificial precursors [30]. We deliberately avoided these expensive procedures to reduce the waste of precursors.

The stoichiometric NM-SG sample suffers a larger Na-loss compared to the solid state one (NM-SS), but the addition of a moderate Na_2CO_3 excess mitigates the sodium deficiency. Notably, NM5-SG and NM10-SG have the same sodium content within the margin of experimental error (±0.01 Na equivalents) despite the different sodium excess used during the synthesis. This could indicate that $Na_{0.92}MnO_2$ is the stoichiometry with the maximum sodium content obtainable by this synthesis method.

Table 2. A summary of the samples synthesized, their synthetic methods and their experimental stoichiometries obtained by EDX.

Sample ID	Synthesis Condition	Na_2CO_3:$Mn(AcO)_2$ Ratio	Nominal Na:Mn Ratio	Experimental Stochiometry
NM-SS	Solid state method	1:2	1:1	$Na_{0.87}MnO_2$
NM-SG	Sol–gel method	1:2	1:1	$Na_{0.81}MnO_2$
NM5-SG	Sol–gel method	1.05:2	1.05:1	$Na_{0.92}MnO_2$
NM10-SG	Sol–gel method	1.1:2	1.1:1	$Na_{0.91}MnO_2$

Experimental XRD of all samples are compared in Figure 1 [39]. The broad background centered around 18° is due to Kapton®. All intense peaks assigned to O3-NMO are observed in all diffractograms, thus confirming a successful preparation route. Moreover, weak additional peaks at 16°, 40.7° and 41.9° were observed. These small peaks could be originated by the minor presence of some manganese oxides or Na_xMnO_2 phases with a lower content of sodium [40], which is in line with the results of EDX. Unfortunately, due to their small number and poor intensity, it is impossible to conduct a clear identification of contaminants.

Upon passing, one may observe that impurities can contribute in slightly modifying the exact stoichiometry of the dominant O3 phase in comparison to the overall composition of each sample (Table 2). Unfortunately, any estimates of the extent of those minor alterations are beyond our experimental capabilities.

The Raman spectra of all samples are shown in Figure 2. Bands around 270, 415, 502, 593 and 645 cm^{-1} can be assigned to O3-NMO [30]. The additional vibrational lines around 212, 309, 366 and 580 cm^{-1} are similar to those observed by Khan et al. [41] in a mixture of O3-$NaMnO_2$/$Na_{0.7}MnO_2$ phases. Overall, by combining evidence from a "bulk-sensitive" technique such as XRD and those from a "surface-sensitive" technique such as MicroRaman, we suggest that all samples are constituted by O3-NMO phases with minor traces of $Na_{0.7}MnO_2$ on the surface of the primary particles. This description is in line with the presence of Na deficiencies evaluated by EDX in the overall composition of samples.

Tuning to sample morphology, SEM micrographs (Figure 3) highlight the presence of well-formed regular prisms of similar shape and particle size modified by the synthesis conditions. The average diameter of the primary particles has been evaluated using ImageJ [37] and estimates are reported on the corresponding micrograph in Figure 3. Sol–gel synthesis leads to smaller primary particles compared to solid state (see NM-SS vs. NM-SG) in the 350–500 nm range. However, the addition of 5% or 10% Na_2CO_3 excess in sol–gel syntheses remarkably promotes crystal growth, leading to much larger particles compared to NM-SG (i.e., 490–860 nm).

Detailed structural features of the O3 structures of the four samples have been obtained by Rietveld Refinement: Fitting results are summarized in Table 3. In Table 4, we compare Mn-O and Na-O bond distances, unit cell volumes, crystal domain sizes, microstrains, antisite defects fraction and Mn mean oxidation states for all samples state.

Table 3. Crystal structure parameters refined by Rietveld optimization for the four samples.

Material	Cell Parameters	Atoms	Wyckoff Positions	Atomic Positions			DW	Occupancies
				x	y	z		
NM-SS (R_w = 2.2%; GOF = 1.47)	a = 5.660 Å	Mn	2*d*	0	0.5	0.5	1.0	1.0
	b = 2.853 Å	Na	2*a*	0	0	0	1.0	0.87
	c = 5.796 Å β = 113.2°	O	4*i*	0.787	0	0.254	1.0	1.0
NM-SG (R_w = 2.0%; GOF = 1.41)	a = 5.664 Å	Mn	2*d*	0	0.5	0.5	1.0	1.0
	b = 2.858 Å	Na	2*a*	0	0	0	1.0	0.81
	c = 5.801 Å β = 113.2°	O	4*i*	0.791	0	0.265	1.0	1.0
NM5-SG (R_w = 2.5%; GOF = 1.66)	a = 5.664 Å	Mn	2*d*	0	0.5	0.5	1.0	1.0
	b = 2.859 Å	Na	2*a*	0	0	0	1.0	0.92
	c = 5.801 Å β = 113.1°	O	4*i*	0.785	0	0.269	1.0	1.0
NM10-SG (R_w = 3.8%; GOF = 2.53)	a = 5.659 Å	Mn	2*d*	0	0.5	0.5	1.0	1.0
	b = 2.858 Å	Na	2*a*	0	0	0	1.0	0.91
	c = 5.792 Å β = 113.1°	O	4*i*	0.812	0	0.320	1.0	0.98

Table 4. Comparison between Mn-O and Na-O distances, unit cell volumes, sizes, strains, estimated antisite defects and Mn mean oxidation state in the four materials.

Material	d_{Mn-O} (Å)	d_{Na-O} (Å)	Volume (Å^3)	$< D_{hkl} >$ (nm)	$< \epsilon >$ (%)	Antisite Defects (%)	Mn ox. State
NM-SS	2.042 (4×) 2.552 (2×)	2.226 (4×) 2.237 (2×)	86.03	70	0.029	19.7	3.13
NM-SG	2.009 (4×) 2.519 (2×)	2.264 (4×) 2.278 (2×)	86.33	99	0.039	23.2	3.19
NM5-SG	2.010 (4×) 2.474 (2×)	2.260 (4×) 2.323 (2×)	86.38	181	0.135	13.7	3.08
NM10-SG	1.841 (4×) 2.377 (2×)	2.454 (4×) 2.474 (2×)	86.15	256	0.212	25.3	3.00

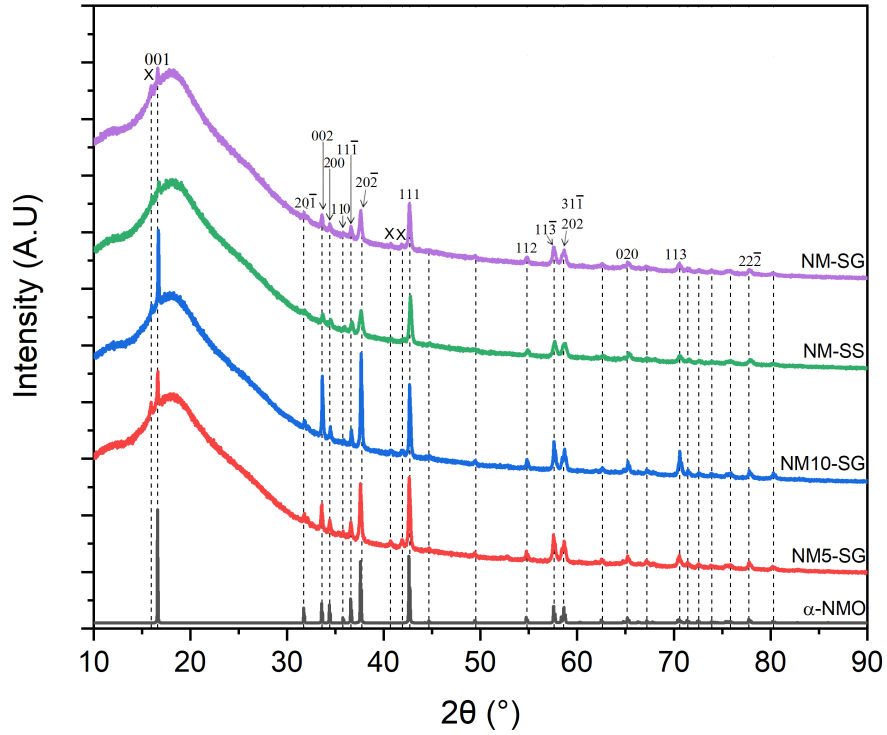

Figure 1. Experimental XRD patterns for all samples compared to theoretical one (α-$NaMnO_2$) calculated by VESTA [39] using structural data from Ref. [30]. Peaks due to impurities are indicated by X.

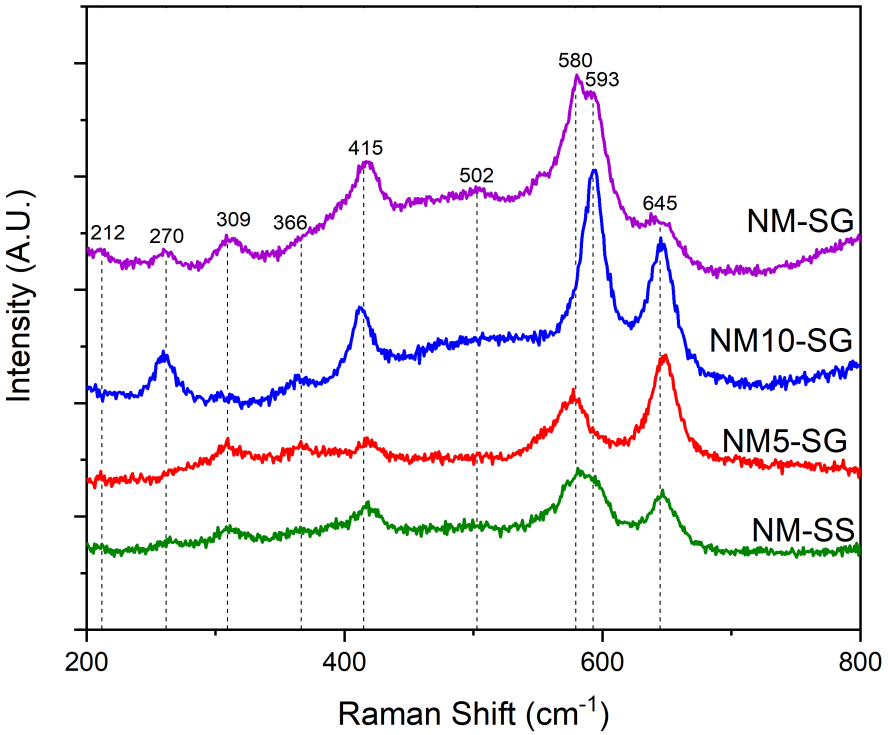

Figure 2. Comparison between the Raman spectra of the four samples.

All materials show very similar cell volume, whereas the crystallite's dimensions increased monotonically from NM-SS to NM-SG, NM5-SG and NM10-SG. Apparently, the addition of Na-excess in the synthesis promotes crystal growth: This evidence is in line with SEM observations. Starting from $< D_{hkl} >$ and $< d >_{SEM}$, it is possible to estimate

the number of crystallites (N_{cr}) in each polycrystalline particle by $(< D_{hkl} > / < d >_{SEM})^3$. Apparently, N_{cr} is much larger for the NM-SS sample compared to all SG materials at 343, 45, 20 and 38 for NM-SS, NM-SG, NM5-SG and NM10-SG, respectively.

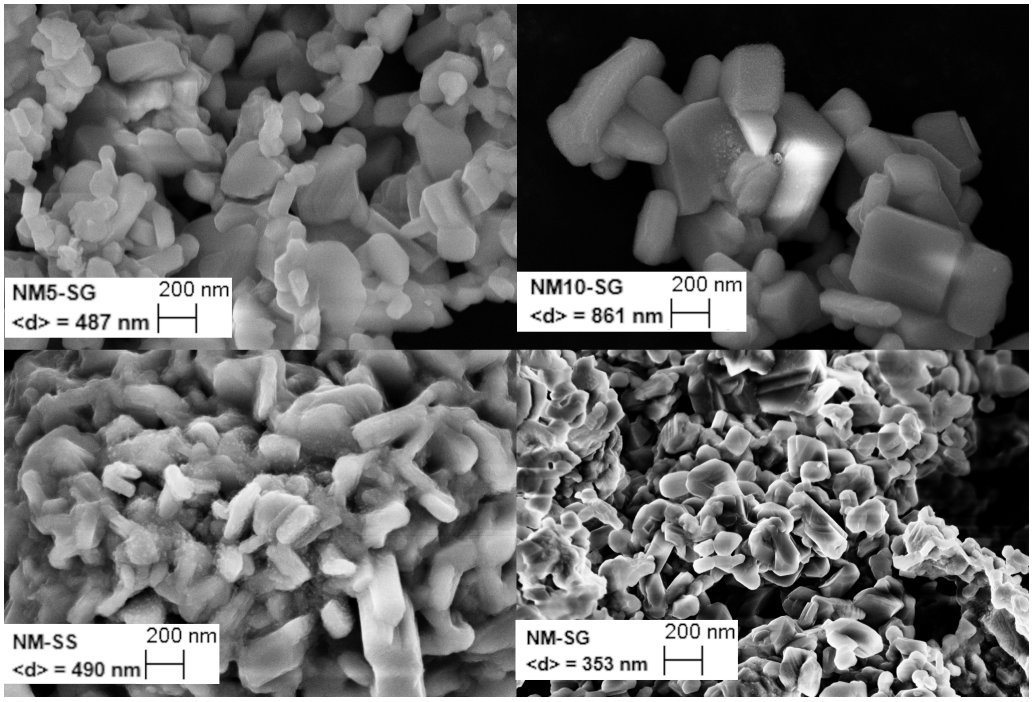

Figure 3. SEM micrographs of the four samples with the average diameter of their respective primary particles (magnifications are identical for all micrographs).

The analysis of bond distances highlights a strong distortion of the MnO_6 octahedra in all materials, caused by the Jahn–Teller effect originated by Mn(III) centers [10]. It is likely that the MnO_6 distortions indirectly alters the octahedral coordination of NaO_6 octahedra. Overall, the changes in the Mn-O/Na-O bond distances apparently show nice correlations with the Mn mean oxidation state and the crystallite's size: larger crystals and larger concentration of Mn^{+3} leads to smaller Mn-O and larger Na-O distances.

Overall, all O3-NMO materials are highly disordered compared to the metal site occupancies and the long-range microstrain. In fact, Mn/Na antisite defect concentrations beyond 13% have been refined by the Rietveld method for all samples. As expected, the microstrain increases while $< D_{hkl} >$ increases, whereas antisite Mn/Na defects show a scattered evolution. Starting from experimental stoichiometries and O3 cell volumes, it is possible to evaluate the empty volume fraction in the unit cells (χ_{voids}). χ_{voids} is calculated as follows:

$$\chi_{voids} = (V_{cell} - Vfill)/V_{cell} \quad (1)$$

and also with the following

$$V_{fill} = (4/3)\pi \cdot 2(r^3_{Na^+} \cdot Occ_{Na} + Occ_{Mn}(r^3_{Mn^{+3}} \cdot \chi_{Mn^{+3}} + r^3_{Mn^{+4}} \cdot \chi_{Mn^{+4}}) + 2 \cdot Occ_O \cdot r^3_{O^{-2}}) \quad (2)$$

assuming for r_{Na^+}, $r_{Mn^{+3}}$, $r_{Mn^{+4}}$ and $r_{O^{-2}}$, which are the Shannon ionic radii [42]. The χ_{voids} estimated includes 35.8%, 36.6%, 35.5% and 36.6% for NM-SS, NM-SG, NM5-SG and NM10-SG, respectively. Apparently, χ_{voids} nicely correlates with antisite defects. On other hand, voids in the structure occur also in parallel to the increase in Na:Mn ratio. In this respect, one may speculate that larger Na content leads to structure induced by larger JT Mn^{+3} ions compared to the non-JT Mn^{+4} ones, thus making the switch between Na^+ and Mn^{+3} easier.

Overall, the larger the crystallites, the larger the strain, whereas we obtain better atomic packing when the antisite defects are smaller.

3.2. Electrochemical Performance

The electrochemical activity of the O3-$NaMnO_2$ has been verified by cyclic voltammetry with a scan rate of 0.05 mV/s. The results are shown in Figure 4. All materials undergo to a similar multi-step redox reaction during sodium intercalation/deintercalation: at least five cathodic/anodic peaks can be easily identified for all samples.

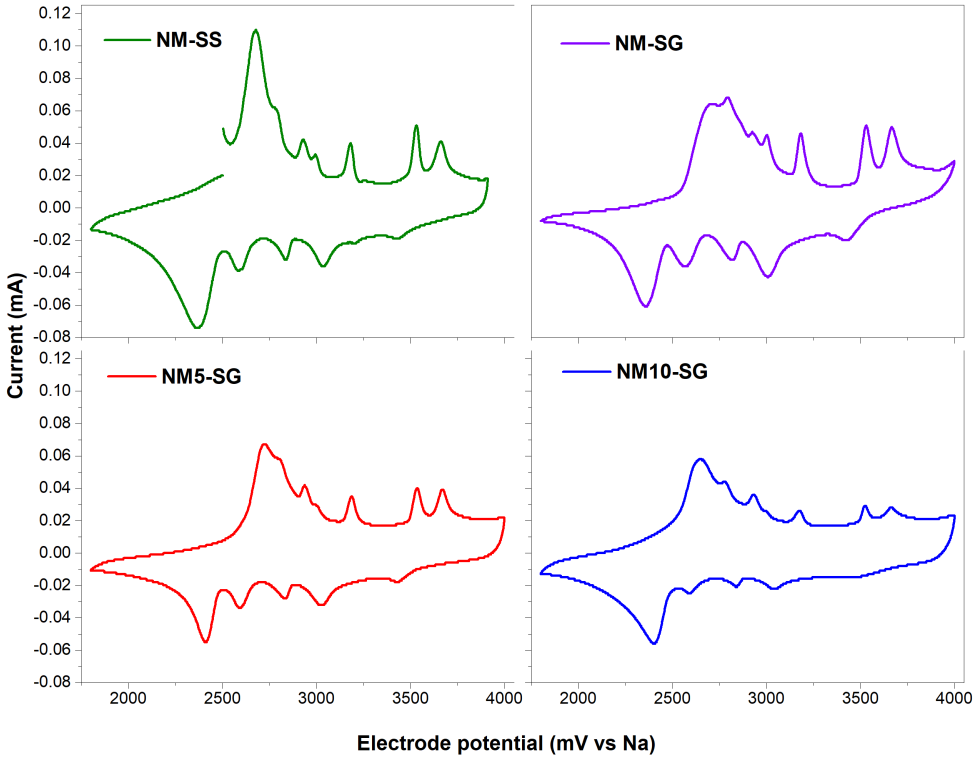

Figure 4. Cyclic voltammetries of the four materials performed with a scan rate of 0.05 mV/s.

The electrochemical performance of the four materials have been investigated in sodium half-cells by galvanostatic tests at 10 mA/g: the working electrode potential profiles are shown in Figure 5. NM-SS achieved both the best charge capacity (211 mAh/g, corresponding to 0.87 Na equivalents deintercalated) and discharge capacity (183 mAh/g, corresponding to 0.75 Na equivalents intercalated). This excellent performance matches the best performance reported in previous studies (see [29–31,35]). NM-SG supplies a similar discharge capacity (179 mAh/g, corresponding to 0.74 Na equivalents intercalated), but remarkably, the charge capacity is smaller, reaching only 154 mAh/g (corresponding to 0.63 Na equivalents deintercalated). This means that the coulombic efficiency in the first cycle is surprisingly larger than 100%. This unexpected evidence likely originates by the large number of Na-vacancies in the pristine O3 lattice (Na occupancy 0.81 (see Table 2)). Thus, after de-sodiation in the first charge, the O3-NMO lattice of the NM-SG sample is capable of re-incorporating larger sodium content by filling the vacant sites in the pristine structure. At the end of the first full cycle, the NM-SG sample has $Na_{0.92}MnO_2$ stoichiometry, which is beyond the pristine one. As a consequence, this material has a larger charge capacity in the second cycle (170 mAh/g, corresponding to 0.70 Na equivalents deintercalated) compared to the first cycle. We confirmed this peculiar behaviour on different synthesis batches. NM5-SG and NM10-SG show much smaller discharge capacities: 144 mAh/g for the former (corresponding to 0.59 Na equivalent intercalated) and 104 mAh/g for the latter (corresponding to 0.43 Na equivalents). These two material are the only ones with a pristine Mn mean oxidation state below 3.1 and with a strongly distorted pristine lattice (i.e., larger crystallites and microstrain). In this respect, we can summarize that well-formed crystallites and small policrystalline aggregates with limited microstrain disclose good

performance in Na-cells, whereas lattice distortions and large crystals are detrimental for electrochemical properties.

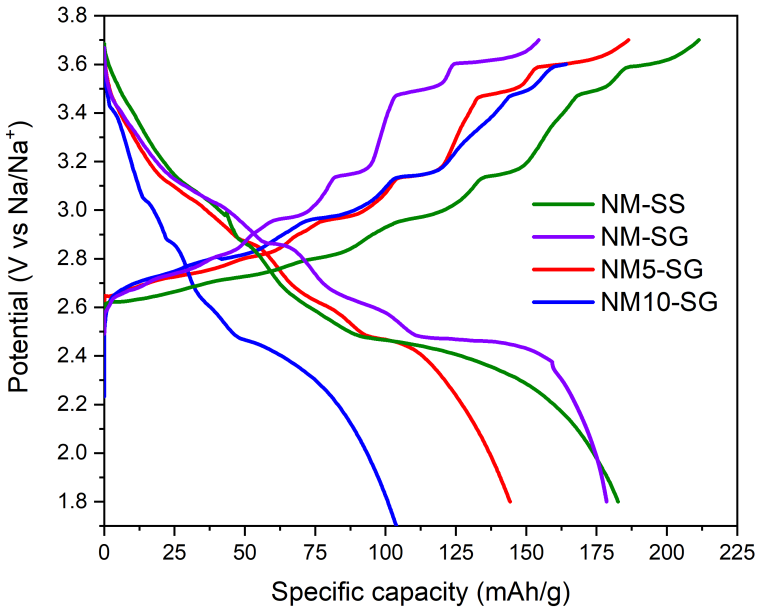

Figure 5. Voltage profile of the four materials during the first charge/discharge cycle.

The performance in repeated charge/discharge cycles are shown in Figure 6. All materials suffer of a constant fade in their performances in line with all previous studies (see Table 1). This decrease is moderate for NM-SS, which is the only material that after 20 cycles still retains a charge/discharge capacity of 130 mAh/g. This performance is comparable to that obtained by Ma et al. [31]). All the other sol–gel materials after 20 cycles show capacities of about 80 mAh/g. Overall, despite the larger tunability of the sol–gel route, the NM-SS sample overcomes the performance of all other materials likely thanks to the smaller defectivity and crystallyte sites. We would like to stress that improvements can be obtained by the further optimization of sol–gel preparation, electrolyte additives or by applying electrode formation procedures. These strategies are under study in our laboratory and will be addressed separately.

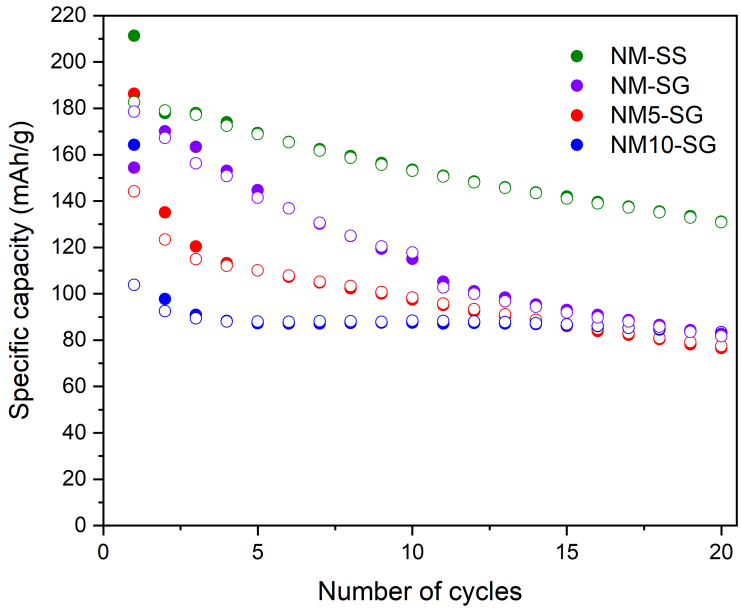

Figure 6. Performance of the four materials during 20 charge/discharge cycles.

3.3. Analysis of the Capacity Fading Mechanism

The performance fading has been further investigated by post mortem Raman spectroscopy and XRD. Samples have been collected after 20 cycles (see Section 2.3 for a detailed description of the procedure used) and characterized ex situ under protective optical windows (transparent glass and Kapton®). The Raman spectra of the post-mortem samples are shown in Figure 7. Apparently, all materials undergo a deep structural evolution during the 20 intercalation/deintercalation cycles. By comparison with reference data [43], we suggest that post mortem spectra belong to a Mn_3O_4-like spinel structure, showing an intense band at 652 cm^{-1}. Only the NM-SS sample shows also an intense Raman band at 578 cm^{-1}, still originating from the pristine O3 lattice. This evidence is a clue of a less-extended structural degradation of surface to the spinel-like lattice. NM-SS structural resilience does not correlate with the sodium content in the pristine lattice (see Table 2), which is similar to the NM5-SG and NM10-SG samples. On other hand, the NM-SS sample shows smaller crystallite site and smaller long-range microstrain compared to all SG synthesis. We may speculate that in order to mitigate the structural degradation of the O3 lattice, it is important to minimize the pristine microstrain and the crystallite size.

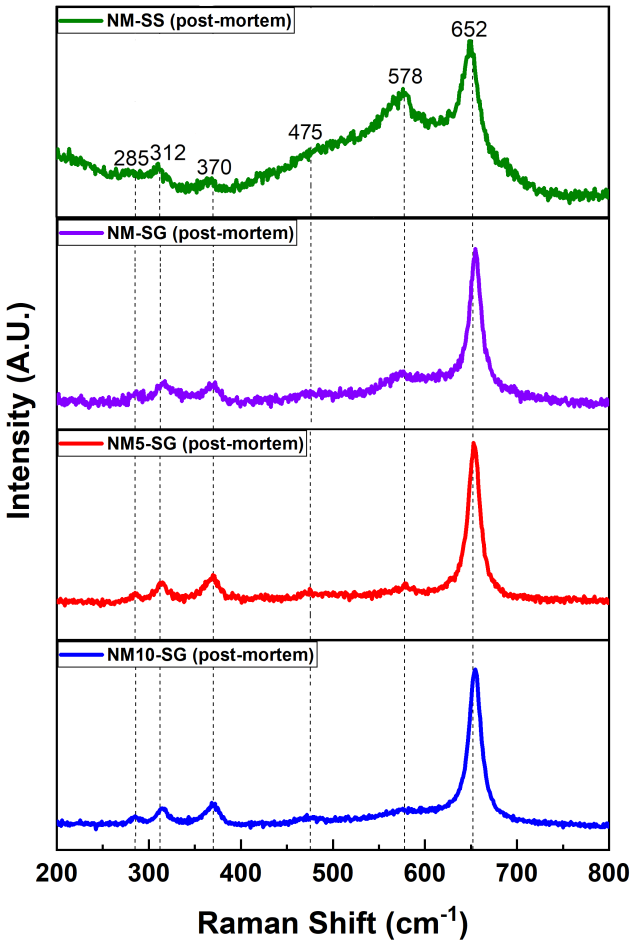

Figure 7. Post mortem Raman spectra of the electrodes after 20 charge/discharge cycles.

After 20 cycles, all four The XRDs of the four post-mortem electrodes are shown in the Figure 8 and compared with the theoretical ones elaborated by VESTA [39], for α-$NaMnO_2$ and Mn_3O_4. The comparison has been limited to the 2θ range 30°–60°, where the differences between the diffraction patterns are remarkable.materials are mainly amorphous, with minimal evidence of pristine O3-structure. Notably, no peaks undoubtedly assignable to the spinel-structure Mn_3O_4 were found.

The combined results by Raman and XRD suggest that, after 20 cycles, all samples comprise poorly crystallized materials likely coated by spinel-like layers.

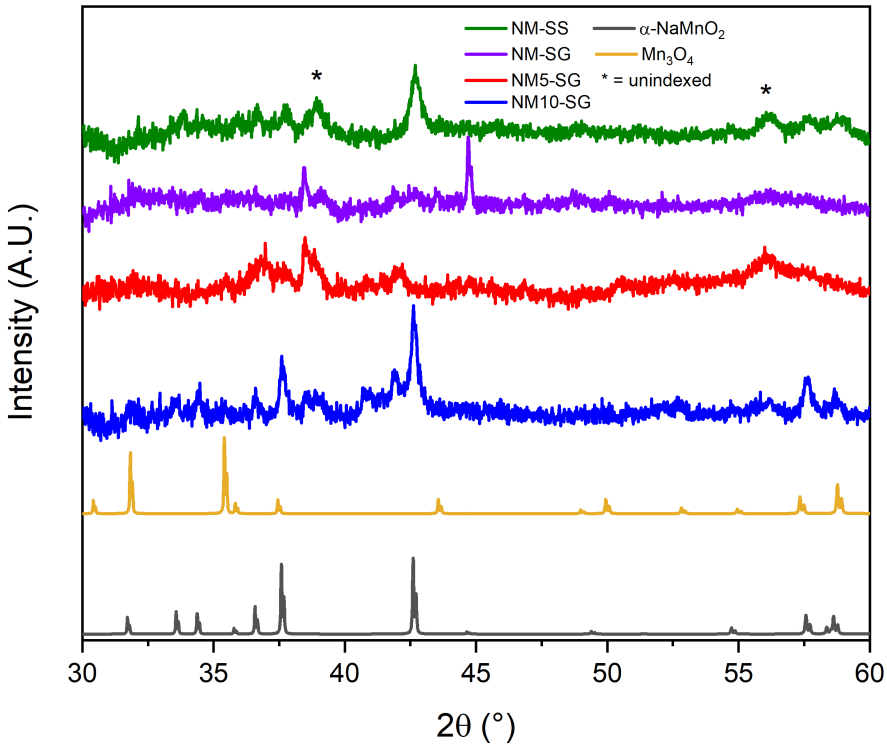

Figure 8. Experimental XRD patterns of post-mortem electrodes made from the four materials compared to theoretical ones (α-$NaMnO_2$ [30] and Mn_3O_4 [44]) calculated by VESTA [39].

To extend the analysis of structural degradations upon charge/discharge, the outperforming NM-SS sample has been submitted to prolonged cycling (see Figure 9a), and the electrode has been collected for post mortem Raman characterization. First of all, the electrochemical performance of the NM-SS sample further deteriorates beyond cycle 20, with a capacity retention of $\sim$ 45% at cycle 70. Notably, in the literature, only Billaud et al. [29] have tested an O3-$NaMnO_2$ in similar prolonged cycling: Our performances are in line with the state-of-the-art results. The Raman spectra after 70 cycles (see Figure 9b) is very difficult to assign, and it is very different in comparison to the ones recorded on the pristine NM-SS and after 20 cycles. Apparently, it resembles "natural tunnel structure manganites" but lacks intense "fingerprint" peaks [45]. However, surprisingly, the spectra does not show, after 70 cycles, any evidence of the spinel lattice. This is direct clue of a further structural transformation and highlights the complexity of the solid state reactivity responsible for the capacity fading mechanism. Qualitatively, one may suggest that the O3-$NaMnO_2$ phase evolves upon cycling in Na-half cells , forming poorly crystallized mixtures of $Na_{0.7}MnO_2/Mn_3O_4$ species followed by a further structural degradation to $Na_{0.1-0.5}MnO_2$ compounds with a tunnel structure. Overall, the fading mechanism is apparently driven by the continuous loss of sodium from the manganese lattice.

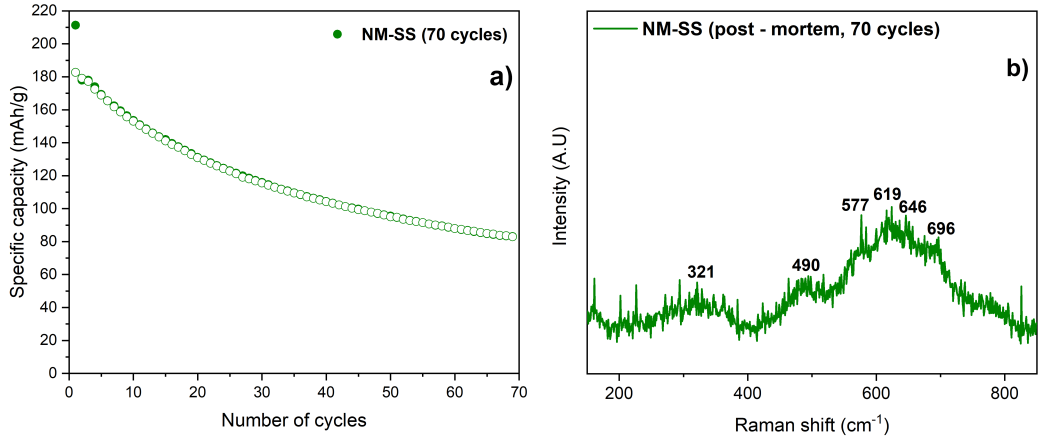

Figure 9. (**a**) Performance of NM-SS during 70 charge/discharge cycles. (**b**) Post mortem Raman spectra of the electrode made from NM-SS after 70 charge/discharge cycles.

4. Conclusions

In this study, we have synthesized four different samples of $NaMnO_2$ using solid state and sol–gel methods and characterized them by physico-chemical and electrochemical approaches. As far as we know, this is the first time reported in the literature that this material is synthesized by sol–gel methods to study the electrochemical features. All materials are constituted by an O3 structure coated by a surface layer of $Na_{0.7}MnO_2$: All of them show the ability to reversibly function as cathodes in sodium-ion batteries. The material synthesized by solid state method (NM-SS) has smaller crystallites and smaller long-range microstrain. These structural features lead to better performance compared to all sol–gel samples. At the same time, the performances of the SG materials suggest that the addition of moderate excesses of sodium in the synthesis hinders performance in cells. All the materials show a capacity fading upon cycling occurring in parallel with the amorphization of the lattices and surface distortion to spinel-like structures. NM-SS shows the best capacity retention thanks to the less-strained pristine lattice.

Author Contributions: Conceptualization, S.B. and A.L.; methodology, S.B.; investigation, M.P., L.S. and A.C.; resources, S.B.; data curation, M.P. and M.T.; writing—original draft preparation M.P.; writing—review and editing, S.B. All authors have read and agreed to the published version of the manuscript.

Funding: Università di Roma La Sapienza—Bando medie attrezzature 2019 rif. "MA21916B755D01C9"; Lazioinnova "Gruppi di ricerca 2020"—POR FESR Lazio 2014–2020 progetto ACTEA "PROT. A0375-2020- 36518".

Institutional Review Board Statement: Not applicable.

Informed Consent Statement: Not applicable.

Data Availability Statement: Data are available upon request addressed by email to the corresponding author.

Conflicts of Interest: The authors declare no conflicts of interest.

References

1. Deng, D. Li-ion batteries: Basics, progress, and challenges. *Energy Sci. Eng.* **2015**, *3*, 385–418. [CrossRef]
2. Liang, Y.; Zhao, C.Z.; Yuan, H.; Chen, Y.; Zhang, W.; Huang, J.Q.; Yu, D.; Liu, Y.; Titirici, M.M.; Chueh, Y.L.; et al. A review of rechargeable batteries for portable electronic devices. *InfoMat* **2019**, *1*, 6–32. [CrossRef]
3. Xu, C.; Dai, Q.; Gaines, L.; Hu, M.; Tukker, A.; Steubing, B. Future material demand for automotive lithium-based batteries. *Commun. Mater.* **2020**, *1*, 99. [CrossRef]
4. Aneke, M.; Wang, M. Energy storage technologies and real life applications—A state of the art review. *Appl. Energy* **2016**, *179*, 350–377. [CrossRef]

5. Stievano, L.; de Meatza, I.; Bitenc, J.; Cavallo, C.; Brutti, S.; Navarra, M.A. Emerging calcium batteries. *J. Power Sources* **2021**, *482*, 228875. [CrossRef]
6. Wang, S.; Sun, C.; Wang, N.; Zhang, Q. Ni- and/or Mn-based layered transition metal oxides as cathode materials for sodium ion batteries: Status, challenges and countermeasures. *J. Mater. Chem. A* **2019**, *7*, 10138–10158. [CrossRef]
7. Liu, Q.; Hu, Z.; Chen, M.; Zou, C.; Jin, H.; Wang, S.; Chou, S.L.; Dou, S.X. Recent Progress of Layered Transition Metal Oxide Cathodes for Sodium-Ion Batteries. *Small* **2019**, *15*, 1805381. [CrossRef]
8. Eftekhari, A.; Kim, D.W. Sodium-ion batteries: New opportunities beyond energy storage by lithium. *J. Power Sources* **2018**, *395*, 336–348. [CrossRef]
9. Zhang, Y.; Zhang, R.; Huang, Y. Air-Stable Na_xTMO_2 Cathodes for Sodium Storage. *Front. Chem.* **2019**, *7*, 335. [CrossRef]
10. Parant, J.P.; Olazcuaga, R.; Devalette, M.; Fouassier, C.; Hagenmuller, P. Sur quelques nouvelles phases de formule Na_xMnO_2 ($x \leq 1$). *J. Solid State Chem.* **1971**, *3*, 1–11. [CrossRef]
11. Mendiboure, A.; Delmas, C.; Hagenmuller, P. Electrochemical intercalation and deintercalation of Na_xMnO_2 bronzes. *J. Solid State Chem.* **1985**, *57*, 323–331. [CrossRef]
12. Delmas, C.; Fouassier, C.; Hagenmuller, P. Structural classification and properties of the layered oxides. *Physica B+C* **1980**, *99*, 81–85. [CrossRef]
13. Caballero, A.; Hernán, L.; Morales, J.; Sánchez, L.; Santos Peña, J.; Aranda, M.A.G. Synthesis and characterization of high-temperature hexagonal P2-$Na_{0.6}MnO_2$ and its electrochemical behaviour as cathode in sodium cells. *J. Mater. Chem.* **2002**, *12*, 1142–1147. [CrossRef]
14. Su, D.; Wang, C.; Ahn, H.j.; Wang, G. Single Crystalline $Na_{0.7}MnO_2$ Nanoplates as Cathode Materials for Sodium-Ion Batteries with Enhanced Performance. *Chem. Eur. J.* **2013**, *19*, 10884–10889. [CrossRef]
15. Jung, E.; Park, Y.; Park, K.; Kwon, M.S.; Park, M.; Sinha, A.K.; Lee, B.H.; Kim, J.; Lee, H.S.; Chae, S.I.; et al. Synthesis of nanostructured P2-$Na_{2/3}MnO_2$ for high performance sodium-ion batteries. *Chem. Commun.* **2019**, *55*, 4757–4760. [CrossRef]
16. Bucher, N.; Hartung, S.; Nagasubramanian, A.; Cheah, Y.; Hoster, H.; Madhavi, S. Layered Na_xMnO_{2+z} in Sodium Ion Batteries-Influence of Morphology on Cycle Performance. *ACS Appl. Mater. Interfaces* **2014**. [CrossRef]
17. Kulka, A.; Marino, C.; Walczak, K.; Borca, C.; Bolli, C.; Novák, P.; Villevieille, C. Influence of Na/Mn arrangements and P2/P′2 phase ratio on the electrochemical performance of Na_xMnO_2 cathodes for sodium-ion batteries. *J. Mater. Chem. A* **2020**, *8*, 6022–6033. [CrossRef]
18. Ma, T.; Xu, G.L.; Zeng, X.; Li, Y.; Ren, Y.; Sun, C.; Heald, S.; Jorne, J.; Amine, K.; Chen, Z. Solid state synthesis of layered sodium manganese oxide for sodium-ion battery by in-situ high energy X-ray diffraction and X-ray absorption near edge spectroscopy. *J. Power Sources* **2017**, *341*, 114–121. [CrossRef]
19. Sehrawat, D.; Rawal, A.; Cheong, S.; Avdeev, M.; Ling, C.D.; Kimpton, J.A.; Sharma, N. Alkali Metal-Modified P2 Na_xMnO_2: Crystal Structure and Application in Sodium-Ion Batteries. *Inorg. Chem.* **2020**, *59*, 12143–12155. [CrossRef]
20. Shibata, T.; Kobayashi, W.; Moritomo, Y. Sodium ion diffusion in layered Na_xMnO_2 (0.49 $\leq$x$\leq$ 0.75): Comparison with Na_xCoO_2. *Appl. Phys. Express* **2014**, *7*, 067101. [CrossRef]
21. Chen, T.R.; Wu, Z.; Xiang, W.; Wang, E.H.; Wu, C.J.; Chen, M.; Guo, X.; Zhong, B.H. The influences of sodium sources on the structure evolution and electrochemical performances of layered-tunnel hybrid $Na_0.6MnO_2$ cathode. *Ceram. Int.* **2017**, *43*, 6303–6311. [CrossRef]
22. Li, J.Y.; Lü, H.Y.; Zhang, X.H.; Xing, Y.M.; Wang, G.; Guan, H.Y.; Wu, X.L. P2-type $Na0.53MnO_2$ nanorods with superior rate capabilities as advanced cathode material for sodium ion batteries. *Chem. Eng. J.* **2017**, *316*, 499–505. [CrossRef]
23. Bucher, N.; Hartung, S.; Franklin, J.B.; Wise, A.M.; Lim, L.Y.; Chen, H.Y.; Weker, J.N.; Toney, M.F.; Srinivasan, M. P2–$Na_xCo_yMn_{1-y}O_2$ (y = 0, 0.1) as Cathode Materials in Sodium-Ion Batteries—Effects of Doping and Morphology To Enhance Cycling Stability. *Chem. Mater.* **2016**, *28*, 2041–2051. [CrossRef]
24. Konarov, A.; Choi, J.U.; Bakenov, Z.; Myung, S.T. Revisit of layered sodium manganese oxides: Achievement of high energy by Ni incorporation. *J. Mater. Chem. A* **2018**, *6*, 8558–8567. [CrossRef]
25. Billaud, J.; Singh, G.; Armstrong, A.R.; Gonzalo, E.; Roddatis, V.; Armand, M.; Rojo, T.; Bruce, P.G. $Na_{0.67}Mn_{1-x}Mg_xO_2$ ($0 \leq x \leq 0.2$): A high capacity cathode for sodium-ion batteries. *Energy Environ. Sci.* **2014**, *7*, 1387–1391. [CrossRef]
26. Lin, Z.; Zhao, S.; Wu, F. Structure and electrochemical properties of layered sodium manganese oxide Na_xMnO_2. *Mater. Res. Express* **2019**, 6, 095509. [CrossRef]
27. Liang, X.; Yu, T.Y.; Ryu, H.H.; Sun, Y.K. Hierarchical O3/P2 heterostructured cathode materials for advanced sodium-ion batteries. *Energy Storage Mater.* **2022**, *47*, 515–525. [CrossRef]
28. Bach, S.; Henry, M.; Baffier, N.; Livage, J. Sol-gel synthesis of manganese oxides. *J. Solid State Chem.* **1990**, *88*, 325–333. [CrossRef]
29. Billaud, J.; Clément, R.J.; Armstrong, A.R.; Canales-Vázquez, J.; Rozier, P.; Grey, C.P.; Bruce, P.G. $\beta-NaMnO_2$: A High-Performance Cathode for Sodium-Ion Batteries. *J. Am. Chem. Soc.* **2014**, *136*, 17243–17248. [CrossRef]
30. Manzi, J.; Paolone, A.; Palumbo, O.; Corona, D.; Massaro, A.; Cavaliere, R.; Muñoz-García, A.B.; Trequattrini, F.; Pavone, M.; Brutti, S. Monoclinic and Orthorhombic $NaMnO_2$ for Secondary Batteries: A Comparative Study. *Energies* **2021**, *14*, 1230. [CrossRef]
31. Ma, X.; Chen, H.; Ceder, G. Electrochemical Properties of Monoclinic NaMnO2. *J. Electrochem. Soc.* **2011**, *158*, A1307. [CrossRef]
32. Guo, S.; Li, Q.; Liu, P.; Chen, M.; Zhou, H. Environmentally stable interface of layered oxide cathodes for sodium-ion batteries. *Nat. Commun.* **2017**, *8*, 135. [CrossRef] [PubMed]

33. Jo, I.H.; Ryu, H.S.; Gu, D.G.; Park, J.S.; Ahn, I.S.; Ahn, H.J.; Nam, T.H.; Kim, K.W. The effect of electrolyte on the electrochemical properties of Na/$\alpha-NaMnO_2$ batteries. *Mater. Res. Bull.* **2014**, *58*, 74–77. [CrossRef]
34. Ma, T.; Xu, G.L.; Li, Y.; Song, B.; Zeng, X.; Su, C.C.; Mattis, W.L.; Guo, F.; Ren, Y.; Kou, R.; et al. Insights into the Performance Degradation of Oxygen-Type Manganese-Rich Layered Oxide Cathodes for High-Voltage Sodium-Ion Batteries. *ACS Appl. Energy Mater.* **2018**, *1*, 5735–5745. [CrossRef]
35. Sato, T.; Sato, K.; Zhao, W.; Kajiya, Y.; Yabuuchi, N. Metastable and nanosize cation-disordered rocksalt-type oxides: Revisit of stoichiometric $LiMnO_2$ and $NaMnO_2$. *J. Mater. Chem. A* **2018**, *6*, 13943–13951. [CrossRef]
36. Toby, B.H.; Von Dreele, R.B. *GSAS-II*: The genesis of a modern open-source all purpose crystallography software package. *J. Appl. Crystallogr.* **2013**, *46*, 544–549. [CrossRef]
37. Schneider, C.A.; Rasband, W.S.; Eliceiri, K.W. NIH Image to ImageJ: 25 years of image analysis. *Nat. Methods* **2012**, *9*, 671–675. [CrossRef]
38. Terayama, K.; Ikeda, M.; Taniguchi, M. Phase Equilibria in the Mn_2O_3-Mn_3O_4-MnO System in CO_2-H_2 Mixtures. *Trans. Jpn. Inst. Met.* **1983**, *24*, 24–28. [CrossRef]
39. Momma, K.; Izumi, F. *VESTA 3* for three-dimensional visualization of crystal, volumetric and morphology data. *J. Appl. Crystallogr.* **2011**, *44*, 1272–1276. [CrossRef]
40. Vaitkus, A.; Merkys, A.; Gražulis, S. Validation of the Crystallography Open Database using the Crystallographic Information Framework. *J. Appl. Crystallogr.* **2021**, *54*, 661–672. [CrossRef]
41. Khan, M.A.; Han, D.; Lee, G.; Kim, Y.I.; Kang, Y.M. P2/O3 phase-integrated $Na0.7MnO_2$ cathode materials for sodium-ion rechargeable batteries. *J. Alloy. Compd.* **2019**, *771*, 987–993. [CrossRef]
42. Database of Ionic Radii. Available online: http://abulafia.mt.ic.ac.uk/shannon/ptable.php (accessed on 18 May 2022).
43. Larbi, T.; Doll, K.; Manoubi, T. Density functional theory study of ferromagnetically and ferrimagnetically ordered spinel oxide Mn_3O_4. A quantum mechanical simulation of their IR and Raman spectra. *J. Alloy. Compd.* **2016**, *688*, 692–698. [CrossRef]
44. Persson, K. Materials Data on Mn_3O_4 (SG:141) by Materials Project. 2014. Available online: https://materialsproject.org/materials/mp-18759/ (accessed on 18 May 2022).
45. Bernardini, S.; Bellatreccia, F.; Casanova Municchia, A.; Della Ventura, G.; Sodo, A. Raman spectra of natural manganese oxides. *J. Raman Spectrosc.* **2019**, *50*, 873–888. [CrossRef]